01 Jan 2022

Plasma Spheroidization of Gas-atomized 304L Stainless Steel Powder for Laser Powder Bed Fusion Process

M. Hossein Sehhat

Austin T. Sutton

Chia-Hung Hung

Ben Brown

et. al. For a complete list of authors, see https://scholarsmine.mst.edu/psmrc_facwork/33

Recommended Citation

Sehhat MH, Sutton AT, Hung CH, et al., 2022, Plasma spheroidization of gas-atomized 304L stainless steel powder for laser powder bed fusion process. Mater Sci Add Manuf, 1(1): 1. https://doi.org/10.18063/msam.v1i1.1

Materials Science in Additive Manufacturing

ORIGINAL RESEARCH ARTICLE

Plasma spheroidization of gas-atomized 304L stainless steel powder for laser powder bed fusion process

M. Hossein Sehhat[1]*, Austin T. Sutton[2], Chia-Hung Hung[3], Ben Brown[4], Ronald J. O'Malley[5], Jonghyun Park[1], Ming C. Leu[1]*

[1]Department of Mechanical and Aerospace Engineering, Missouri University of Science and Technology, Rolla, MO 65409, USA

[2]Los Alamos National Laboratory, Los Alamos, NM 87545, USA

[3]Department of Mechanical Engineering, National Cheng Kung University, Tainan, Taiwan

[4]Materials Engineering, Kansas City National Security Campus, Kansas City, MO 64147, USA

[5]Department of Materials Science and Engineering, Missouri University of Science and Technology, Rolla, MO 65409, USA

Abstract

Particles of AISI 304L stainless steel powder were spheroidized by the induction plasma spheroidization process (TekSphero-15 spheroidization system) to assess the effects of the spheroidization process on powder and part properties. The morphology of both as-received and spheroidized powders was characterized by measuring particle size and shape distribution. The chemistry of powders was studied using inductively coupled plasma optical emission spectroscopy for evaluation of composing elements, and the powder's microstructure was assessed by X-ray diffraction for phase identification and by electron backscattered diffraction patterns for crystallography characterization. The Revolution Powder Analyzer was used to quantify powder flowability. The mechanical properties of parts fabricated with as-received and spheroidized powders using laser powder bed fusion process were measured and compared. Our experimental results showed that the fabricated parts with plasma spheroidized powder have lower tensile strength but higher ductility. Considerable changes in powder chemistry and microstructure were observed due to the change in solidification mode after the spheroidization process. The spheroidized powder solidified in the austenite-to-ferrite solidification mode due to the loss of carbon, nitrogen, and oxygen. In contrast, the as-received powder solidified in the ferrite-to-austenite solidification mode. This change in solidification mode impacted the components made with spheroidized powder to have lower tensile strength but higher ductility.

Keywords: Powder characteristics; Mechanical properties; Plasma spheroidization; Laser powder bed fusion; Additive manufacturing; 304L stainless steel

***Corresponding authors:**
M. Hossein Sehhat (hsehhat@mst.edu)
Ming C. Leu (mleu@mst.edu)

Citation: Sehhat MH, Sutton AT, Hung CH, *et al*., 2022, Plasma spheroidization of gas-atomized 304L stainless steel powder for laser powder bed fusion process. *Mater Sci Add Manuf,* 1(1): 1. https://doi.org/10.18063/msam.v1i1.1

Received: February 4, 2022

Accepted: February 23, 2022

Published Online: March 18, 2022

1. Introduction

Additive manufacturing (AM) is poised to revolutionize the way components are created by enabling the construction of complex geometries and allowing more freedom and flexibility during the design process[1,2]. AM can unify all the steps of a conventional

manufacturing method, including forming, machining, welding, and assembling, into a single-step process[3-6]. Advanced AM processes, such as laser foil printing (LFP) and fused deposition modeling (FDM), have been developed to fabricate complex-geometry metal parts with high mechanical properties[7-11]. The widespread use of AM has primarily benefited the aerospace industry by fabricating 3-dimensional (3D) parts using metals[12,13]. As the powder-based AM technology has matured, the criticality of the powder used has become increasingly apparent, especially in the laser powder bed fusion (LPBF) process with its special thermal history conditions[14-16]. LPBF uses a wiper to spread a layer of powder with a typical thickness ranging 30 – 100 μm on the substrate to be scanned by the laser according to the computer-aided design (CAD) data provided by the part geometry in a layer-by-layer fashion[17]. The powder's ability to properly spread on the substrate when being pushed by the wiper significantly affects the powder bed density, which consequently affects the porosity and mechanical properties of the fabricated parts[18]; in addition, these might impact the tensile strengths and fracture toughness of fabricated parts[19,20].

The powder flowability strongly depends on the geometry of powder particles[21]. The irregular particle geometries tend to engage, agglomerate, and interlock together, hindering the powder flow. In contrast, spherical particles show better flowability, mainly due to the absence of inter-particle friction forces[22]. Therefore, to have a better powder flowability, the delivered powder feedstock to the LPBF machine should be in spherical geometries[23].

The commonly used powder feedstock in the LPBF process is currently produced using inert gas atomization. The molten material, generated through induction melting, is atomized by an inert gas, such as argon or nitrogen, when falling under gravity in the atomization chamber[24,25]. Although most of the produced gas-atomized powder particles are in acceptable spherical geometries, the presence of a few irregular particles is still easily observable. Therefore, improving the properties of gas-atomized powder by creating even more spherical particles without the appearance of irregular geometries is crucial.

Plasma spheroidization changes the geometries of powder particles by creating surface tensions when subjecting the particles to plasma around 10,000 K, which is high enough to melt and decompose most materials[26]. Due to this process' considerable benefits, such as improving particle geometries and reducing chemical impurities, several researchers have recently studied the plasma spheroidization process, a comprehensive review of which has been conducted by Sehhat *et al.* [27]. Wang *et al.*[28] took advantage of the high temperature in the spheroidization process to produce spherical tungsten particles since the gas atomization method was not found capable of generating the required high temperature to meet tungsten's high melting point. In another study, an increase in ferrite volume fraction, generation of nano-sized particles, and an increase in powder-bed density due to finer particles filling the inter-particle voids were observed by Ji *et al.*[29] through investigating the spheroidization impacts on AISI stainless steel 316L powder. Depending on the type of raw material, which may be the powder of a pure metal or a multi-element alloy, the evaporation rate per element during the spheroidization process would be different due to the different melting points and vapor pressures of constitutive elements. The different reaction of constitutive elements to high temperatures changes the chemical composition of yielded spheroidized powder compared to its as-received condition. In a study conducted by Park *et al.*[30], the best set of process parameters for the spheroidization of AISI stainless steel 316 powder was analyzed. A slight decrease in the particle size and a considerable increase in powder flowability were observed. Although these previous studies present valuable knowledge on the spheroidization process for improving powder properties, a substantial knowledge gap still exists on the relationship between powder's chemical composition before the LPBF process and part properties after the LPBF process. Such lack of knowledge creates ambiguity in terms of the morphological, chemical, and microstructural properties of the powder feedstock. The work presented in this paper covers these gaps with a significant focus on tailoring the powder properties with plasma spheroidization for use in the LPBF process.

In this study, the gas-atomized AISI 304L stainless steel powder, composed of Fe, Ni, Cr, Mn, and Si, was spheroidized by an induction plasma spheroidization process to investigate the impact of this process on powder characteristics and part properties. The spheroidized powder was characterized in morphology, chemistry, and microstructure, which were compared with those of the as-received powder. Some parts were fabricated with the spheroidized powder using the LPBF process. Their mechanical properties were compared with those of the parts fabricated with the as-received powder to assess the effects of the spheroidization process on the mechanical properties of LPBF parts.

2. Material and methods

2.1. Material

The gas-atomized (in argon media) AISI 304L stainless steel powder was provided by LPW Technology (Carpenter Technology Corp., USA). The manufacturer reported the particle size distribution of as-received powder as 13, 20, and 30 μm for D_{10}, D_{50}, and D_{90}, respectively.

2.2. Plasma spheroidization

An inductively coupled plasma (ICP) system, TekSphero-15 (Tekna Plasma System Inc., Canada), was utilized with a maximum power capacity of 15 kW. The machine was equipped with Tekna's PN-35M induction plasma torch, operating at the 2 – 5 MHz frequency range.

Figure 1 shows an illustration of the plasma spheroidization process where powder with irregular particle geometries is injected into a high-temperature plasma (3000 – 10,000 K) under an inert atmosphere (argon) to get melted[26]. The surface tension effects on the molten liquid droplets reshape the particles to spheres while the particles fall under gravity inside the water-cooled processing chamber[31]. The molten particles would be solidified at high cooling rates (~10^6 K/s) and deposited in the main collection bin. To successfully spheroidize powder, several parameters (including the sheath, central, carrier, and hydrogen gas flow rates), the power delivered to the plasma, and the powder mass flow rate can be adjusted. The parameters used in this study are listed in Table 1.

2.3. Part fabrication

The used LPBF machine was a Renishaw AM250 (Renishaw plc., UK), capable of fabricating parts with complex geometries from a range of metal powders. This machine is equipped with a high-precision fiber laser (70 µm focal diameter) in 200 W power and a build volume of 250 × 250 × 300 mm^3. Before feeding the powder into the LPBF machine, the Renishaw powder recovery system (sieving to particle size <63 µm) was used to eliminate the larger particles that may result from the agglomeration of particles during powder handling. For the experiment of part fabrication, the variable factor was the powder type: as-received versus spheroidized. The response variables were mechanical properties in terms of yield strength (YS), ultimate tensile strength (UTS), and strain at break. As shown in Figure 2, to evaluate the repeatability of tensile properties, 15 cubic specimens with 10 mm edge dimension were built per powder (as-received and spheroidized) using the Renishaw AM250 machine, where X-axis is the powder spreading direction and Z-axis is the part building direction. All the 15 cubic specimens per powder type were fabricated in one build. The LPBF process parameters were chosen based on the reported results of building fully dense parts with the least energy input[32], which are listed in Table 2.

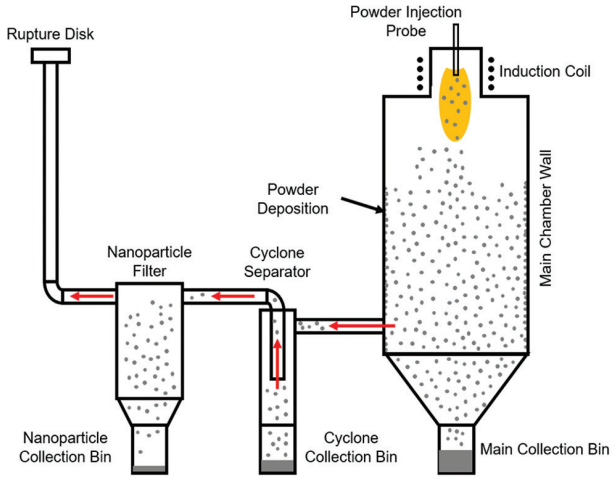

Figure 1. Schematic of the TekSphero-15 showing the injection of the powder into the plasma.

2.4. Characterization techniques

Analyzing powder particles using image analysis of scanning electron microscope (SEM) micrographs is a popular method among researchers because of these images' reliability. SEM images can be used to determine particle size distributions and analyze particle geometries[33]. The morphology of powder was studied through analysis of micrographs taken by ASPEX SEM (Aspex Corp., USA). The change in the shape of powder particles was quantified using the aspect ratio, defined as the ratio of the major axis to the minor axis of the bounding ellipse for each particle[34]. Through this definition, the particle sphericity increases as the aspect ratio approaches unity.

The method of ICP optical emission spectroscopy (ICP-OES) was deployed to study powder chemistry. The microstructures of powder particles were analyzed by the electron backscattered diffraction (EBSD) probe provided

Table 1. Process parameters for spheroidizing 304L SS powder in a TekSphero-15 system

Power	Gas flow rates			
	Carrier	Central	Sheath	Hydrogen
12 kW	4 lpm	10 lpm	40 lpm	2 lpm

Table 2. Process parameters used for part fabrication in Renishaw AM250

Parameter	Value
Laser power (W)	200
Spot diameter (µm)	70
Point distance (µm)	70
Exposure time (µs)	88
Scan speed (m/s)	0.8
Hatch spacing (µm)	85
Layer thickness (µm)	50

by the FEI Helios NanoLab 600 (Thermo Fisher Scientific, USA); samples of as-received and spheroidized powders were set in conductive bakelite, mechanically polished down to 0.05 µm, and vibratorily polished in 0.02 µm colloidal silica for 4 h. The phase identification of powder was performed using X-ray diffraction (XRD).

The dynamic powder flow properties were measured and analyzed using a Revolution Powder Analyzer (Mercury Scientific Inc., USA). As demonstrated in Figure 3, this analyzer rotates a drum composed of a powder sample. The drum has glasses on both sides, which let the coaxial camera take images of the powder movement to quantify flowability when the powder is illuminated with a backlight on the opposite side. While rotating, the powder will occasionally avalanche as it succumbs to the force of gravity, where it eventually comes to rest. At the onset of slumping, the angle is known as the avalanche angle and is calculated at the cycle's peak. The break energy can be used to evaluate the amount of energy needed to begin each avalanche and is the subtraction of the maximum powder's energy level before an avalanche begins from the starting powder's energy level before starting the rotation process. A standard rotational speed recommended by the equipment's manufacturer is 0.3 rpm, which was used to observe powder flow for the as-received and spheroidized 304L powders.

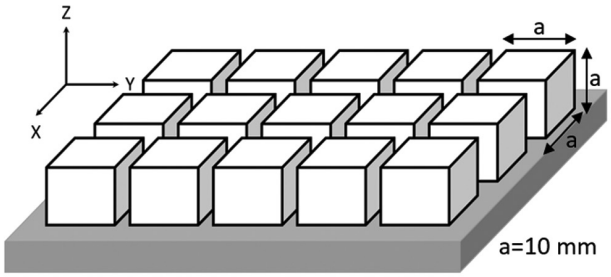

Figure 2. Schematic of specimens built with the Renishaw AM250.

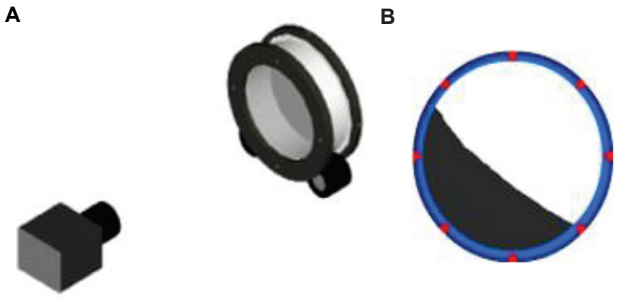

Figure 3. Illustration of powder flowability test measured by the Revolution Powder Analyzer. (A) The rotating drum watched by a digital camera. (B) The side-view of rotating drum with a powder sample in the beginning of an avalanche cycle[35].

The tensile properties of parts fabricated with as-received and spheroidized powders were measured using an Instron 5969 Dual Column Universal Testing System (Instron, USA) with 50 kN force capacity at a strain rate 0.015/min. To evaluate the repeatability of tensile properties per each fabricated part, 5 mini-tensile specimens (with thickness 1 ± 0.02 mm and dimensions shown in Figure 4) were cut from each cube and tested using a universal Instron machine at room temperature with a crosshead speed of 0.015/min[36]. The analysis of variance (ANOVA) was conducted on the obtained results of tensile tests.

3. Results and discussion

3.1. Powder morphology

The SEM micrographs provided in Figure 5 indicate the morphological differences between as-received and plasma spheroidized powders, where particles with irregular geometries in the as-received powder

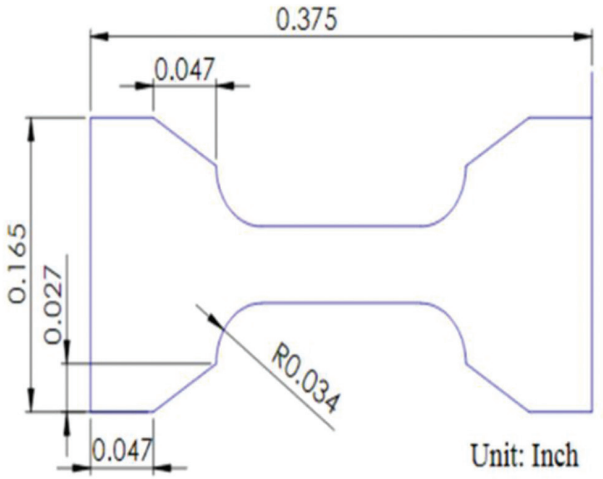

Figure 4. Dimensions of mini-tensile test specimens with thickness 1 ± 0.02 mm (taken from[37]).

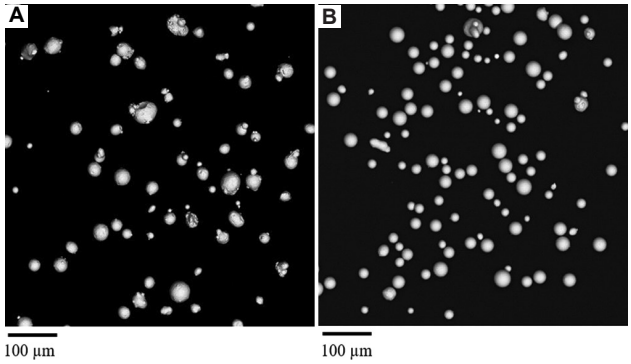

Figure 5. SEM micrographs of AISI 304L stainless steel powder in (A) as-received and (B) spheroidized conditions.

were altered to almost complete spheres after the spheroidization process.

The particle size distributions obtained from 1200 particles of the as-received and spheroidized powders shown in Figure 6 indicate that the as-received powder was primarily reshaped by spheroidization, rather than reduced in size by vaporization or enlarged through the agglomeration of molten particles during solidification. This invariation in size is further evidenced by the lack of change in the 10th, 50th, and 90th cumulative percentiles of the particle size distributions in Figure 6 and their values in Table 3. This nearly identical particle size for the as-received and spheroidized 304L powders is desirable as it indicates the advantage of the spheroidization process in improving the particle geometries while keeping the particle size constant.

Also, the plasma spheroidization improved the uniformity of the as-received powder for particles below 30 µm, which exhibited higher sphericity. Since a particle size of 30 µm is close to the D_{90} of the spheroidized powder, the results in Figure 7 indicate that at least 90% of the particles by number distribution showed enhancements in the particle shape. To further demonstrate the improvement in sphericity, the cumulative aspect ratio distributions of the as-received and spheroidized powders were compared, revealing that the spheroidization process drastically reduced the maximum asperity of 90% of the particles from approximately 1.8 to 1.2.

Table 3. Cumulative percentiles of particle size distributions in Figure 6 comparing the as-received and spheroidized powders

Sample	D_{10} (µm)	D_{50} (µm)	D_{90} (µm)
As-received	13.41 ± 0.03	19.9 ± 0.01	30.4 ± 0.04
Spheroidized	13.6 ± 0.02	20.4 ± 0.02	31.3 ± 0.06

3.2. Powder chemistry

The possible impact of the plasma spheroidization process on the material's bulk chemistry is another crucial aspect that should also be considered. Table 4 shows the bulk chemistries of as-received and spheroidized powders, obtained through a combination of ICP-OES and inert gas fusion to determine the heavy and light alloying elements, respectively. Comparing the bulk chemistries before and after spheroidization reveals that the wt% of each Mn, C, and N, which are volatile elements within AISI 304L stainless steel powder, reduced during the plasma spheroidization process due to vaporization. However, it should be noted that despite these changes in chemistry, the spheroidized powder still lies within the AISI specifications for 304L stainless steel.

The chrome-nickel equivalency was determined using the WRC-1992[38] model for insight into differences in the solidification behavior, and the obtained data are included in Table 4. An increase in the chrome-nickel equivalency (Cr_{eq}/Ni_{eq}) from 1.50 to 1.74 due to plasma spheroidization was found. Based on the work done by Korinko *et al.*[39] on the solidification behavior of stainless steels under welding conditions, a shift from austenite-to-ferrite (AF) solidification mode to ferrite-to-austenite (FA) solidification mode is therefore expected due to the chemistry change. As such, parts produced using as-received powder will solidify as primary austenite and secondary delta ferrite. In contrast, the spheroidized powder will produce a microstructure that exhibits primary ferrite with secondary austenite after solidification. The ramifications of such change in

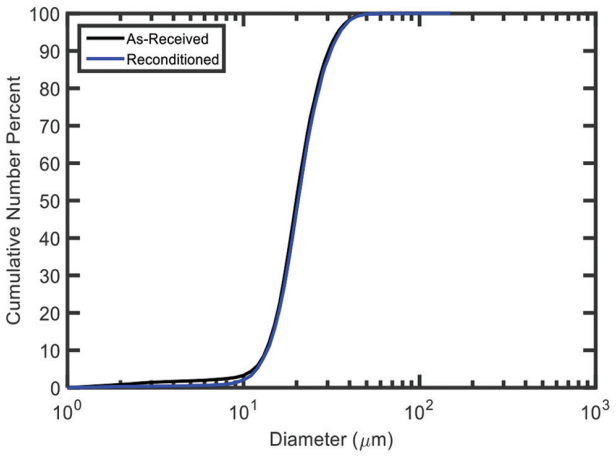

Figure 6. Particle size distributions of the as-received and spheroidized AISI 304L stainless steel powder.

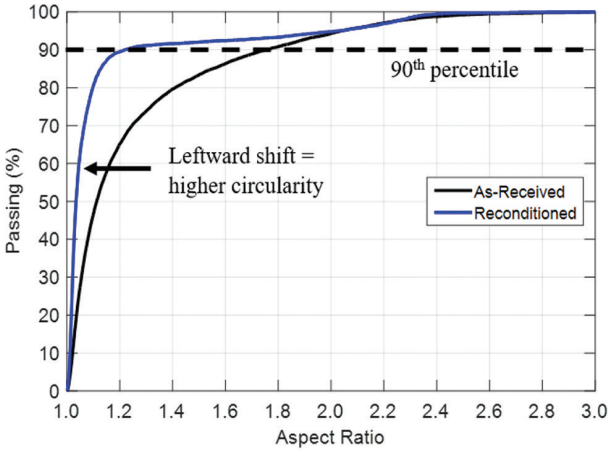

Figure 7. Particle shapes of as-received and spheroidized powders, quantified using the aspect ratio.

Table 4. Bulk chemistry of as-received and spheroidized powders.

Type of powder	Element (wt%)									
	Fe	Cr	Ni	Mn	Si	C	S	O	N	Cr_{eq}/Ni_{eq}
As-received	69.9	18.28	9.04	1.27	0.56	0.015	0.005	0.027	0.07	1.50
Spheroidized	70.0	18.18	9.41	0.83	0.56	0.008	0.004	0.024	0.03	1.74
AISI specifications	-	18 – 20	8 – 12	2 max	1 max	0.03 max	0.03 max	-	-	-

the solidification behavior are discussed in section **3.3** regarding the microstructures of powder and part.

In order to see the impact of the spheroidization process on the ordinary impurities in stainless steel, the oxygen and nitrogen contents of both as-received and spheroidized 304L powders were measured using elemental evaluation of metals through inert gas fusion. Figure 8 compares the oxygen and nitrogen contents of powder before and after the spheroidization process. The oxygen content was found to reduce with plasma processing slightly. Reduction of oxygen content is a desirable result as this means that the processing conditions employed did not add any further oxygen to the powder. The nitrogen content in the powder drastically decreased after the spheroidization process, which improved the purity of the feedstock. Thus, spheroidizing 304L powder is beneficial for reducing impurities, making this powder more suitable for the LPBF process.

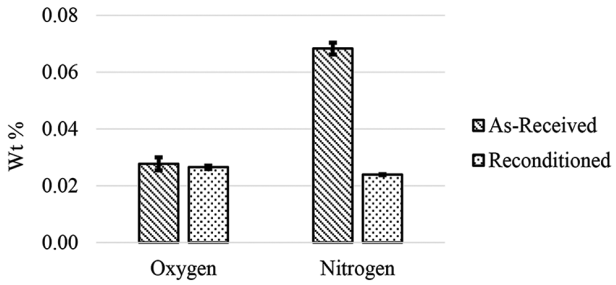

Figure 8. Oxygen and nitrogen content of as-received and spheroidized 304L powders.

3.3. Microstructure

Changes in the bulk chemistry of the powder with plasma spheroidization were manifested in the powder microstructure. The microstructures of as-received and spheroidized 304L powders were investigated using XRD and EBSD. As shown in Figure 9, the XRD patterns of as-received and spheroidized powder particles were compared. While the as-received powder only contains face-centered cubic (FCC; γ), the spheroidized powder diffraction pattern displays a mixture of both FCC and body-centered cubic (BCC; δ) phases. While the FCC phase indicates austenite, identification of the BCC phase is more convoluted due to the similarity in the diffraction patterns of martensite (BCT) and delta ferrite (BCC). Although a martensitic transformation is promoted with high cooling rates achievable in plasma spheroidization, martensite requires carbon to form. Since the spheroidized powder's carbon content in Table 4 is very low (0.008%), martensite formation is suppressed, suggesting that the ferrite BCC phase is retained and could not wholly transform to austenite during the rapid solidification of particles.

The EBSD results, including the distributions of austenite (in blue color) and delta ferrite (in red color), are shown in Figure 10. The as-received powder is predominantly

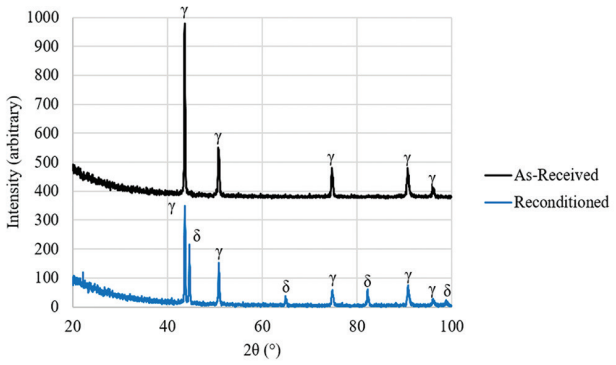

Figure 9. XRD diffraction patterns of as-received and spheroidized powders.

austenite with few delta ferrite traces within the bulk of particles, indicative of an austenite-ferrite (AF) solidification mode. It should be noted that the Cr_{eq}/Ni_{eq} of the as-received powder (see Table 4), determined from the bulk chemistry, is close to the boundary between AF and FA solidification modes[39]. Thus, solidification as primary austenite followed by some ferrite formation is possible and is corroborated by the small volume of ferrite present within the particles.

The changes in powder microstructure resulted from plasma spheroidization are a consequence of the increase in Cr_{eq}/Ni_{eq}. It should be noted that although the concentration of the heavy elements (Fe, Cr, Ni, Si) are unchanged, the lighter elements, including C and N, decrease substantially. Since C and N are potent austenitic stabilizers, even minor deviations in the concentrations of both alloying elements can lead to vastly different microstructures. Thus,

vaporization of C and N during spheroidization increased the Cr_{eq}/Ni_{eq} ratio, promoting FA solidification mode (Figure 11). Since the cooling rate of particles during plasma spheroidization is large, primary ferrite cannot undergo a solid-state transformation to austenite. The competition between austenite and delta ferrite phases within steel depends on the material chemistry and the cooling rate.

Moreover, the cooling rate increases with decreasing particle size, providing variation in the microstructure in polydisperse powders. Kelly *et al.*[40] studied the size-dependent microstructure of 303 stainless steel droplets with sizes ranging from 20 to 120 µm. They concluded that the smallest particles were predominantly BCC, whereas the largest particles contained an FCC microstructure. The increase in BCC, or delta ferrite, with decreasing particle size, was a consequence of enhanced supercooling. Moreover, since small particles have the lowest probability of containing potent nucleants, large undercooling can be reached before solidification begins. Since the enthalpy of BCC crystallization is less than FCC, ferrite is more prone to solidification before austenite in smaller particles. The conclusions provided by Kelly *et al.* coupled with the bulk chemistry of the powder suggest that plasma spheroidization increases the chrome-nickel equivalency of the input material, which solidifies as a combination of ferrite and austenite.

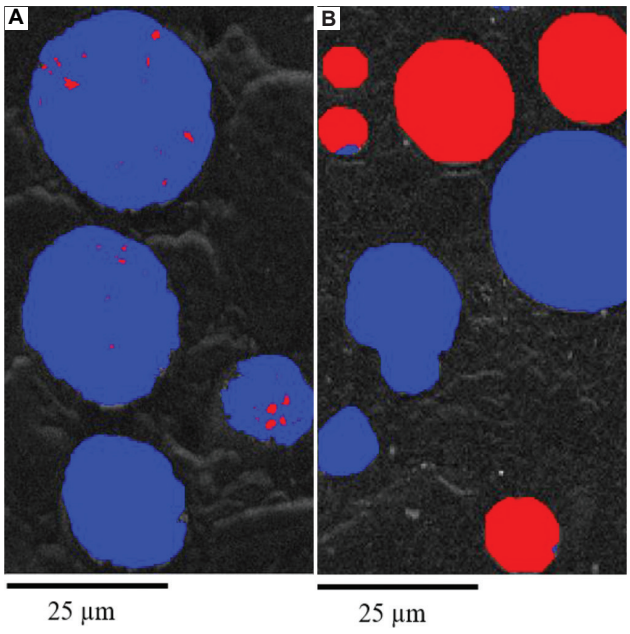

Figure 10. EBSD phase patterns of (A) as-received and (B) spheroidized 304L powders. The blue phase corresponds to austenite and the red phase to delta ferrite. The spheroidized powder is found to contain a larger amount of delta ferrite.

3.4. Flowability

Table 5 provides the results of the Revolution Powder Analyzer flowability test. The avalanche angle and break energy measurements were repeated 150 times, and the means and standard deviations were calculated. Due to the larger avalanche angle and break energy of the as-received powder over the spheroidized powder, it is concluded that the spheroidized powder has higher flowability than the as-received powder. This data suggests that the as-received material is more cohesive due to its larger asperity (as shown in Figure 7).

3.5. Characterization of fabricated parts

Figure 12 presents the results of tensile tests, and Table 6 shows their mean and standard deviations. Performing an ANOVA with a significance level of 0.05 showed that the YS, UTS, and strain at break of as-received and reconditioned powders are significantly different ($P < 0.0001$). The parts fabricated with the spheroidized powder had lower YS and UTS than those of the as-received powder by approximately 70 and 30 MPa, respectively, while their strain at break was higher by about 0.2. The lower strength and higher ductility follow the chemistry change in the powder, i.e., reduction in N, C, Cr, and O, and these results agree with the studies reported in the literature. By investigating the effects of N content on stainless steel powders during the plasma spheroidization process, Razumov *et al.*[41] found that the reduction in N content (which is an austenite stabilizer) decreased the tensile properties of fabricated parts. Wang *et al.*[42] assessed the effects of chemical composition on tensile properties of austenitic stainless steels. They found that

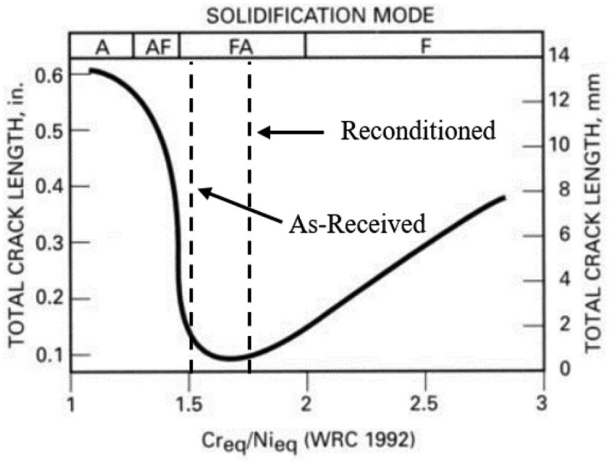

Figure 11. Weld crack length of austenitic stainless steel vs. chrome-nickel equivalency (taken from[39]). The spheroidized powder has a higher chrome-nickel equivalency than the as-received powder.

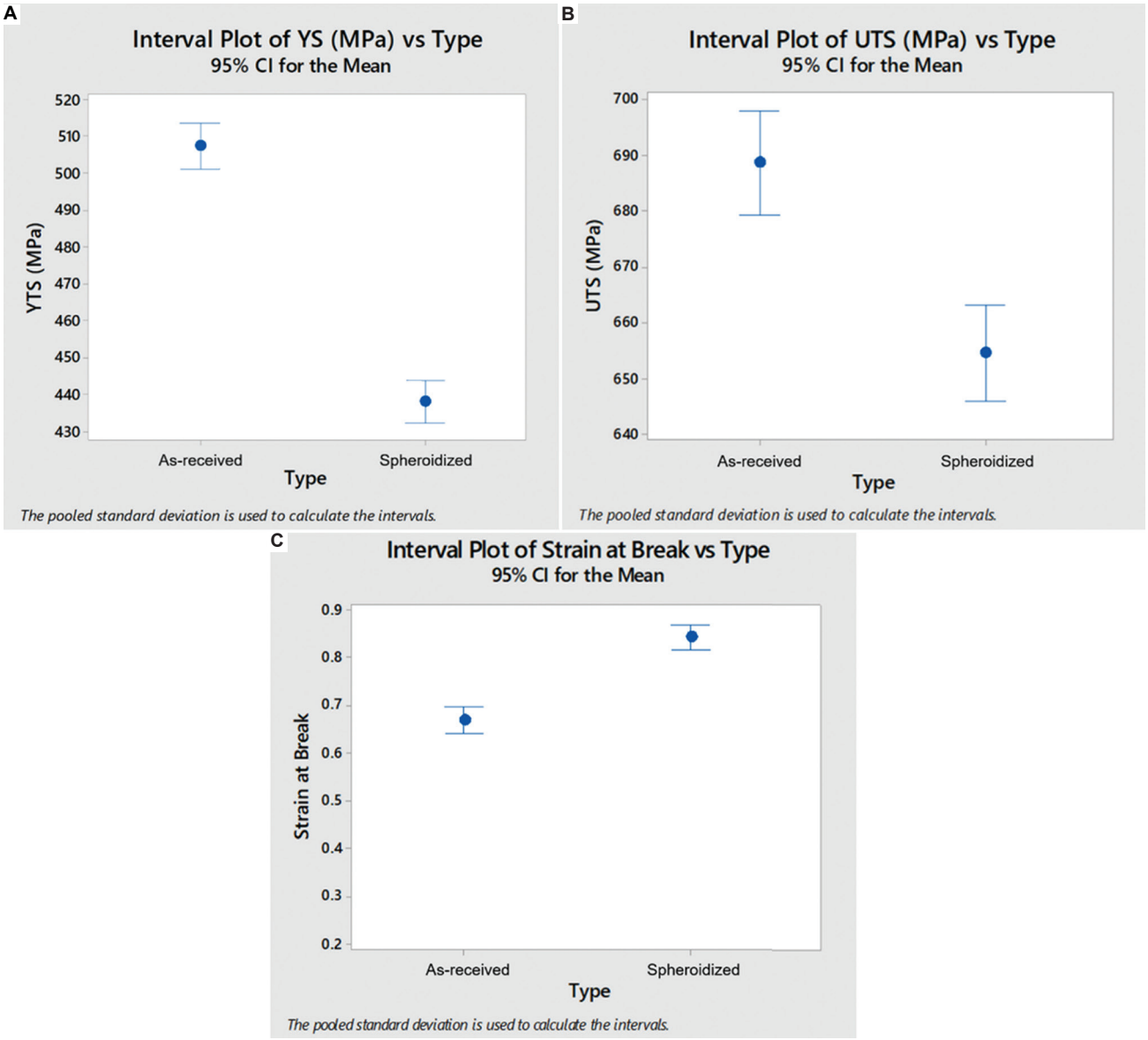

Figure 12. Comparison of the tensile properties of parts built using as-received and spheroidized powders. (A) Yield strength. (B) Ultimate tensile strength. (C) Strain at break.

the reduction in C and Cr decreased the tensile properties of fabricated parts. It is known that C and Cr are usually added to the austenite stainless steels to stabilize the austenite and to create and disperse carbides. They also reported that lower oxygen leads to increased ductility. Thus, the higher ductility of the parts fabricated with the spheroidized powder can be attributed to reduced oxygen content in the spheroidized powder.

Two representative samples of typical fracture surfaces of parts built with the as-received and spheroidized powders are shown in Figure 13. The ductility difference between the 2 parts is readily apparent, as evidenced by the larger area reduction in the part made with the spheroidized powder[43]. The results of density measurement using Archimedes method for the fabricated parts with the as-received and spheroidized powders were not statistically significantly different ($P > 0.05$) with a mean density of 7.93 g/mL. The lack of pores in the fractographs and the minimal change in density suggest that the stark difference in ductility is not due to pores. Instead, the tensile response of the materials is a consequence of the chemistry and the resulting microstructure. As mentioned before, one of the significant differences in the chemistry of the 2 powders was found in the nitrogen content. Using this knowledge, JMatPro[44]

simulations were performed by varying the powder's nitrogen content to predict its influence on the material strength. Figure 14 compares the strength and hardness of the as-received and spheroidized materials predicted by JMatPro simulations, with the only difference being in the nitrogen content (as discussed in Table 4). A decrease in the strength of material is predicted. While this difference may not be as large as the one found in the tensile test results, the simulations indicate that reduction in nitrogen can reduce the strength of austenitic stainless steels.

Table 5. Flowability comparison using the Revolution Powder Analyzer for as-received and spheroidized 304L powders.

Sample	Avalanche angle (°)	Break energy (mJ/kg)
As-received	45.4 ± 1.5	43.2 ± 5.1
Spheroidized	42.4 ± 0.8	28.7 ± 1.2

Table 6. Variation in mechanical properties of fabricated parts with as-received and spheroidized powders.

Property	Type	Mean	Standard deviation
YS (MPa)	As-received	507.27	14.55
	Spheroidized	438.18	18.61
UTS (MPa)	As-received	688.71	19.76
	Spheroidized	654.61	11.18
Strain at break	As-received	0.66	0.044
	Spheroidized	0.84	0.06

YS: Yield strength; UTS: Ultimate tensile strength.

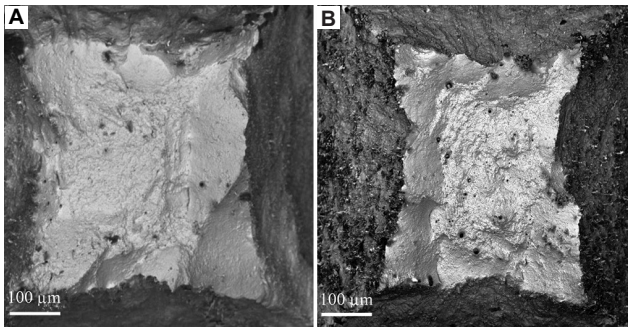

Figure 13. Fractographs of parts built using (A) as-received and (B) spheroidized powder.

From SEM micrographs of some cross-sections on the x-z plane (Figure 15) for investigating the microstructure, it can be observed that the parts built with the as-received powder (Figure 15A **and** B) are mostly comprised of a cellular microstructure all around the melt pool. However, the parts built with spheroidized powder (Figure 15C **and** D) exhibit cellular microstructure only at the melt pool boundaries. In contrast, a sharp transition to a featureless region towards the center of the melt pool develops.

Moreover, as the chrome-nickel equivalency decreased, the amount of cellular microstructure within the weld increased due to a shift toward primary austenite solidification. Therefore, using identical process parameters, the proportion of cellular and featureless regions in Figure 15 is controlled by powder chemistry. As the chrome-nickel equivalency increased, the ratio of the featureless phase to the cellular phase increased, hinting at a change in the solidification mode. It should be noted that the featureless and cellular phases indicate FA and AF solidification modes, respectively, as denoted in the SEM images in Figure 15. Therefore, the increase in the chrome-nickel equivalency of the powder during plasma spheroidization agrees well with the observed increase in the part's featureless phase. As mentioned in the previous discussion of the particle microstructure, the decrease in C and N caused the chrome-nickel equivalency to increase from 1.50 to 1.74 (Table 4). Therefore, the drastic change in the part microstructure results from a change in the powder chemistry, shifting the solidification mode from AF to FA. When investigating the powder, the solidification path difference led to a large undercooling of particles

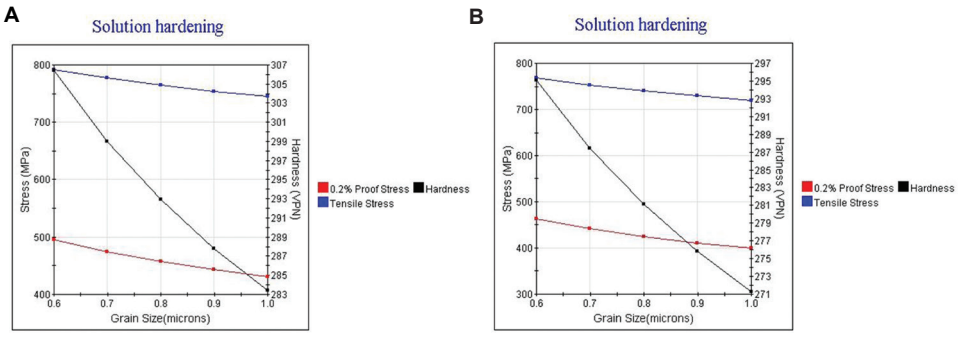

Figure 14. Strength and hardness of (A) as-received and (B) spheroidized powder.

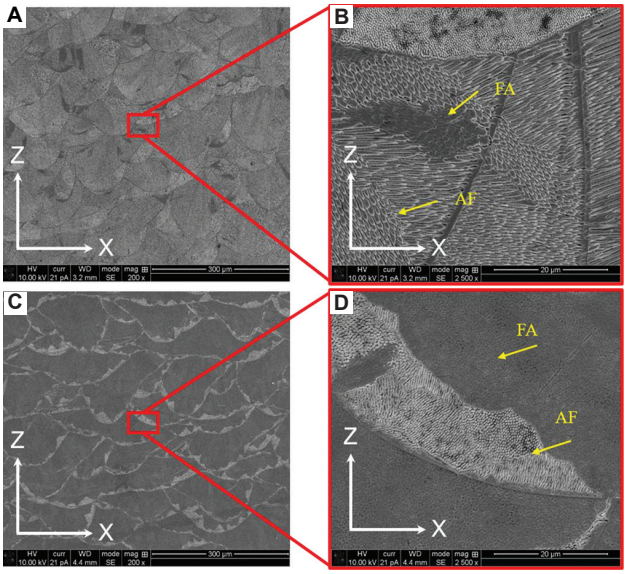

Figure 15. SEM micrographs of parts built with (A-B) as-received and (C-D) spheroidized powder. The samples were electrolytically etched using a 60%/40% nitric acid to water solution.

during spheroidization, promoting delta ferrite formation. Therefore, it is critical to assess if the change in powder chemistry leads to delta ferrite retention in the as-built microstructure, which is a future work of this study.

In addition to causing a difference in the resulting microstructure, a reduction in C and N can decrease the strength since the reduction of both alloying elements prevents the material from solid solution strengthening. Moreover, the removal of the dislocation-dense cellular structure through FA solidification will also reduce the strength. Thus, the lower strength of the parts produced with the spheroidized powder compared to the as-received powder is expected.

4. Conclusion

After the plasma spheroidization process, the particles reshaped to spheres while their particle size remained essentially unchanged. This indicates the particles are only reshaping in geometry but not changing in particle size. The reduction of solid solution strengthening elements including carbon and nitrogen after the spheroidization process changed the solidification mode of powder particles and fabricated parts. The spheroidized powder contained partially ferritic particles, increasing the powder's overall ferrite content compared to the as-received powder. The parts made with the spheroidized powder exhibited a FA solidification mode. The reduction in solid solution strengthening elements including nitrogen and carbon, as well as oxygen content, accompanied by the changes in solidification mode influenced the properties of parts built with the spheroidized powder, which exhibited a lower strength but higher ductility than the parts fabricated with the as-received powder. The more spherical geometry of the spheroidized powder improved the powder's flowability compared to the as-received powder.

Acknowledgments

This work was funded by Honeywell Federal Manufacturing & Technologies LLC under Contract No. DE-NA0002839 with the U.S. Department of Energy. The publisher, by accepting the article for publication, acknowledges that the United States Government retains a nonexclusive, paid-up, irrevocable, worldwide license to publish or reproduce the published form of this manuscript, or allow others to do so, for the United States Government purposes.

Conflict of interest

The authors declare that they have no conflict of interest.

Author contributions

Conceptualization: M. Hossein Sehhat, Austin T. Sutton

Data curation: M. Hossein Sehhat, Austin T. Sutton, Chia-Hung Hung

Investigation: M. Hossein Sehhat, Austin T. Sutton, Chia-Hung Hung, Ben Brown, Ronald J. O'Malley, Jonghyun Park, Ming C. Leu

Formal analysis: M. Hossein Sehhat, Austin T. Sutton, Chia-Hung Hung, Ben Brown

Funding acquisition: Ming C. Leu

Supervision: Ming C. Leu

Writing – original draft: M. Hossein Sehhat, Austin T. Sutton

Writing – review & editing: M. Hossein Sehhat, Austin T. Sutton, Chia-Hung Hung, Ben Brown, Ronald J. O'Malley, Jonghyun Park, Ming C. Leu

Availability of data and materials

The raw or processed data required to reproduce these findings cannot be shared at the time of article publication as the data also forms part of an ongoing study.

References

1. Committee F42 on Additive Manufacturing Technologies. Available from: https://www.astm.org/COMMITTEE/F42.htm [Last accessed on 2021 Jan 02].

2. Behdani B, Senter M, Mason L, *et al.*, 2020, Numerical study on the temperature-dependent viscosity effect on the strand shape in extrusion-based additive manufacturing. *J Manuf Mater Process*, 4: 46.

https://doi.org/10.3390/jmmp4020046

3. Sehhat MH, Mahdianikhotbesara A, Hadad M, 2022, Formability investigation for perforated steel sheets. *Int J Mater Manuf*, 15: 12.

https://doi.org/10.4271/05-15-02-0012

4. Mahdianikhotbesara A, Sehhat MH, Hadad M, 2022, A numerical and experimental study into thermal behavior of micro friction stir welded joints of Al 1050 and copper sheets. *Adv Mater Res*, 15: 1–15.

5. Mahdianikhotbesara A, Sehhat MH, Hadad M, 2021, Experimental study on micro-friction stir welding of dissimilar butt joints between Al 1050 and pure copper. *Metallogr Microstruct Anal*, 10: 1–16.

https://doi.org/10.1007/S13632-021-00771-5

6. Yadegari F, Sehhat MH, Mahdianikhotbesara A, 2022, A Numerical Study of Automotive Body Panel Draw Dies Defects Using Finite Element Simulation. *Research Square*.

https://doi.org/10.21203/RS.3.RS-1300589/V1

7. Sehhat MH, Behdani B, Hung CH, *et al*., 2021, Development of an empirical model on melt pool variation in laser foil printing additive manufacturing process using statistical analysis. *Metallogr Microstruct Anal*, 1: 1–8.

https://doi.org/10.1007/S13632-021-00795-X

8. Hung CH, Turk T, Sehhat MH, *et al*., 2022, Development and experimental study of an automated laser-foil-printing additive manufacturing system. *Rapid Prototyp J*, ahead-of-print.

https://doi.org/10.1108/RPJ-10-2021-0269

9. Turk T, Hung CH, Sehhat MH, *et al*., 2021, Methods of Automating the Laser-Foil-Printing Additive Manufacturing Process. International Solid Freeform Fabrication Symposium, University of Texas at Austin.

10. Sehhat MH, Mahdianikhotbesara A, Yadegari F, 2021, Impact of temperature and material variation on mechanical properties of parts fabricated with fused deposition modelling (FDM). *Int J Adv Manuf Technol*, 2021: 107984.

https://doi.org/10.21203/RS.3.RS-1079840/V1

11. Sehhat MH, Mahdianikhotbesara A, Yadegari F, 2021, Verification of Stress Transformation in Anisotropic Material Additively Manufactured by Fused Deposition Modeling (FDM). Free Download Manager.

https://doi.org/10.21203/RS.3.RS-1107949/V1

12. Hung CH, Chen WT, Sehhat MH, *et al*., 2020, The effect of laser welding modes on mechanical properties and microstructure of 304L stainless steel parts fabricated by laser-foil-printing additive manufacturing. *Int J Adv Manuf Technol*, 1: 1-11.

https://doi.org/10.1007/s00170-020-06402-7

13. Jirandehi AP, Khonsari MM, 2021, General quantification of fatigue damage with provision for microstructure: A review. *Fatigue Fract Eng Mater Struct*, 1: 13515.

https://doi.org/10.1111/ffe.13515

14. Liu T, Lough CS, Sehhat H, *et al*., 2021, *In-Situ* Thermographic Inspection for Laser Powder Bed Fusion. In: 2021 International Solid Freeform Fabrication Symposium, University of Texas at Austin.

15. Nezhadfar PD, Thompson S, Saharan A, *et al*., 2021, Fatigue and failure analysis of an additively manufactured contemporary aluminum alloy. In: The Minerals, Metals and Materials Series. Springer Science and Business Media Deutschland GmbH, Berlin. p212–219.

https://doi.org/10.1007/978-3-030-65396-5_31

16. Sehhat MH, Mahdianikhotbesara A, Yadegari F, 2021, Experimental validation of conductive heat transfer theory: Thermal resistivity and system effects. *Comput. Res Prog Appl Sci Eng*, 7(1): 1–6.

https://doi.org/10.52547/crpase.7.4.2415

17. Sehhat MH, Sutton AT, Hung CH, *et al*., 2021, Investigation of mechanical properties of parts fabricated with gas- and water-atomized 304L stainless steel powder in the laser powder bed fusion process. *JOM*, 2021: 1–8.

https://doi.org/10.1007/S11837-021-05029-7

18. Sehhat MH, Mahdianikhotbesara A, 2021, Powder spreading in laser-powder bed fusion process. *Granul Matter*, 23: 89.

https://doi.org/10.1007/s10035-021-01162-x

19. Kumar P, Jayaraj R, Zhu Z, *et al*., 2022, Role of metastable austenite in the fatigue resistance of 304L stainless steel produced by laser-based powder bed fusion. *Mater Sci Eng A*, 837: 142744.

https://doi.org/10.1016/J.MSEA.2022.142744

20. Kumar P, Zhu Z, Nai SM, *et al*., 2021, Fracture toughness of 304L austenitic stainless steel produced by laser powder bed fusion. *Script Mater*, 202: 114002.

https://doi.org/10.1016/J.SCRIPTAMAT.2021.114002

21. Kurzynowski T, Chlebus E, Kuźnicka B, *et al*., 2012, Parameters in Selective Laser Melting for Processing Metallic Powders. *Proc SPIE*, 2012: 823914.

https://doi.org/10.1117/12.907292

22. Muñiz-Lerma JA, Nommeots-Nomm A, Waters KE, *et al*., 2018, A comprehensive approach to powder feedstock characterization for powder bed fusion additive manufacturing: A case study on AlSi7Mg, *Materials* (*Basel*), 11: 2386.

https://doi.org/10.3390/ma11122386

23. Sun P, Fang ZZ, Zhang Y, *et al*., 2017, Microstructure and mechanical properties of Ti-6Al-4V fabricated by selective laser melting of powder produced by granulation-sintering-deoxygenation method. *JOM*, 69: 2731–2737.

https://doi.org/10.1007/S11837-017-2584-3

24. Antony LV, Reddy RG, 2003, Processes for production of high-purity metal powders. *JOM*, 55: 14–18.

    https://doi.org/10.1007/s11837-003-0153-4

25. Rafi AH, Ahmed DH, 2022, Two-dimensional analogies to the deformation characteristics of a falling droplet and its collision. *Arch Mech Eng*, 69: 21–43.

    https://doi.org/10.24425/ame.2021.139649

26. Dolbec R, Boulos M, Bouchard E, *et al*., 2013, Nanopowders synthesis at industrial-scale production using the inductively-coupled plasma technology. In: Proceeding International Conference Advanced Nanotechnology for Environmental Engineering. p21–24.

    https://doi.org/10.1109/ICANMEET.2013.6609224

27. Sehhat MH, Chandler J, Yates Z, 2021, A review on ICP powder plasma spheroidization process parameters. *Int J Refract Met Hard Mater*, 2021: 105764.

    https://doi.org/10.1016/J.IJRMHM.2021.105764

28. Wang JJ, Hao JJ, Guo ZM, *et al*., 2015, Preparation of spherical tungsten and titanium powders by RF induction plasma processing. *Rare Met*, 34: 431–435.

    https://doi.org/10.1007/s12598-014-0293-4

29. Ji L, Wang C, Wu W, *et al*., 2017, Spheroidization by plasma processing and characterization of stainless steel powder for 3D printing. *Metall Mater Trans A Phys Metall Mater Sci*, 48: 4831–4841.

    https://doi.org/10.1007/s11661-017-4240-5

30. Park JY, Park KB, Kang JW, *et al*., 2020, Spheroidization behavior of water-atomized 316 stainless steel powder by inductively-coupled thermal plasma. *Mater Today Commun*, 2020: 101488.

    https://doi.org/10.1016/j.mtcomm.2020.101488

31. Li YL, Ishigaki T, 2004, Spheroidization of titanium carbide powders by induction thermal plasma processing. *J Am Ceram Soc*, 84: 1929–1936.

    https://doi.org/10.1111/j.1151-2916.2001.tb00939.x

32. Pan T, Karnati S, Zhang Y, *et al*., 2020, Experiment characterization and formulation estimation of tensile properties for selective laser melting manufactured 304L stainless steel. *Mater Sci Eng A*, 798: 140086.

    https://doi.org/10.1016/j.msea.2020.140086

33. Vigneau E, Loisel C, Devaux MF, *et al*., 2000, Number of particles for the determination of size distribution from microscopic images. *Powder Technol*, 107: 243–250.

    https://doi.org/10.1016/S0032-5910(99)00192-8

34. Strondl A, Lyckfeldt O, Brodin H, *et al*., 2015, Characterization and control of powder properties for additive manufacturing. *JOM*, 67: 549–554.

    https://doi.org/10.1007/s11837-015-1304-0

35. Revolution Powder Analyzer Mercury Scientific Inc, (n.d.). Available from: http://www.mercuryscientific.com/instruments/revolution-powder-analyzer [Last accessed on 2021 Jan 02].

36. Najafizadeh N, Rajabi M, Hashemi R, Amini S, 2019, Improved microstructure and mechanical properties of sheet metals in ultrasonic vibration enhanced biaxial stretch forming. *J Theor Appl Vibr Acoust*, 5: 1–10.

    https://doi.org/10.22064/tava.2019.102421.1124

37. Karnati S, Hoerchler JL, Liou F, *et al*., 2017, Influence of Gage Length on Miniature Tensile Characterization of Powder Bed Fabricated 304L Stainless Steel. International Solid Freeform Fabrication Symposium.

38. Hilton ZT, Newkirk JW, O'malley RJ, 2017, Studying Chromium and Nickel Equivalency to Identify Viable Additive Manufacturing Stainless Steel Chemistries. International Solid Freeform Fabrication Symposium.

39. Korinko PS, Malene SH, 2001, Considerations for the weldability of types 304L and 316L stainless steel. *J Fail Anal Prev*, 1: 61–68.

    https://doi.org/10.1007/BF02715336.

40. Kelly TF, Cohen M, Sande JB, 12984, Rapid Solidification of a Droplet-processed Stainless Steel. *Metall Trans A Phys Metall Mater Sci*, 15: 819–833.

    https://doi.org/10.1007/BF02644556

41. Razumov NG, Popovich AA, Wang Q, 2018, Thermal plasma spheroidization of high-nitrogen stainless steel powder alloys synthesized by mechanical alloying. *Met Mater Int*, 24: 363–370.

    https://doi.org/10.1007/s12540-018-0040-8

42. Wang Y, Wu X, Li X, *et al*., 2020, Prediction and analysis of tensile properties of austenitic stainless steel using artificial neural network. *Metals* (*Basel*), 10: 234.

    https://doi.org/10.3390/met10020234

43. Jirandehi AP, Mehdizadeh M, Khonsari MM, 2020, Temperature-induced buckling of ductile metals during cyclic loading and the subsequent early fracture. *Int J Mech Sci*, 176: 105525.

    https://doi.org/10.1016/j.ijmecsci.2020.105525

44. Sente Software JMatPro®, (n.d.). Available from: https://www.sentesoftware.co.uk/jmatpro [Last accessed on 2014 Jan 04].